Preventing the Capillary-Induced Collapse of Vertical Nanostructures

Tanmay Ghosh, Eva-Corinna Fritz, Deepan Balakrishnan, Ziyu Zhang, Nandi Vrancken, Utkarsh Anand, Hong Zhang, N. Duane Loh, XiuMei Xu,* Frank Holsteyns, Christian A. Nijhuis,* and Utkur Mirsaidov*

Read Online

ACCESS | Metrics & More | Article Recommendations | SI Supporting Information

ABSTRACT: Robust processes to fabricate densely packed high-aspect-ratio (HAR) vertical semiconductor nanostructures are important for applications in microelectronics, energy storage and conversion. One of the main challenges in manufacturing these nanostructures is pattern collapse, which is the damage induced by capillary forces from numerous solution-based processes used during their fabrication. Here, using an array of vertical silicon (Si) nanopillars as test structures, we demonstrate that pattern collapse can be greatly reduced by a solution-phase deposition method to coat the nanopillars with self-assembled monolayers (SAMs). As the main cause for pattern collapse is strong adhesion between the nanopillars, we systematically evaluated SAMs with different surface energy components and identified H-bonding between the surfaces to have the largest contribution to the adhesion. The advantage of the solution-phase deposition method is that it can be implemented before any drying step, which causes patterns to collapse. Moreover, after drying, these SAMs can be easily removed using a gentle air-plasma treatment right before the next fabrication step, leaving a clean nanopillar surface behind. Therefore, our approach provides a facile and effective method to prevent the drying-induced pattern collapse in micro- and nanofabrication processes.

KEYWORDS: high-aspect-ratio nanostructures, pattern collapse, capillary forces, silane, self-assembled monolayers
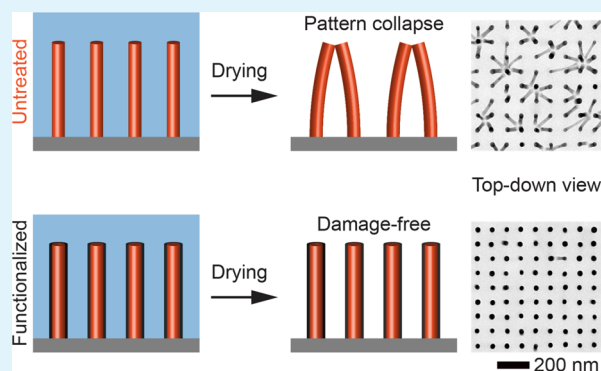
High-aspect-ratio (HAR) vertical nanostructures are important for many technologies, such as solar cells,[1,2] biomedical sensors,[3] and microelectronics.[4] In particular, using vertical nanowires to build scalable three-dimensional (3D) transistors is considered one of the most viable approaches to increase the density, efficiency, and speed of nanodevices.[5,6] However, the fabrication of these nanowires involves multiple solution-based processes (*e.g.*, wet etching[7] and cleaning[8]), and these fragile nanostructures are prone to damage because of the capillary forces.[4,9−16] Specifically, during drying, these nanowires tend to bend because of capillary forces and stick to each other.[17] More importantly, this damage persists even after the complete evaporation of the liquid, with the nanowires remaining permanently clustered due to adhesion between them.[18−20]

A common method to reduce micro- and nanoscale pattern collapse is to lower capillary forces causing their bending. For example, the use of low-surface-tension liquids, such as isopropyl alcohol (IPA), can decrease the capillary forces, but this approach shows limited improvement for moderate aspect ratio nanostructures.[17,21−23] When the aspect ratio increases further, an even lesser force can cause the same deflection, and IPA cannot prevent the collapse of the HAR

nanostructures, as we will show later. Supercritical drying is an effective method where the temperature and pressure of the environment are increased above the critical point, and the liquid goes to the supercritical phase. As a result, the nanostructures do not experience any capillary force.[24,25] However, this method is not well suited for high-throughput fabrication processes required by the semiconductor industry, and consequently, it is hard to integrate supercritical drying into a fabrication process flow.[26] Vapor-phase surface chemistry modification has also been used to prevent pattern collapse.[27−31] However, this process has limited application in the cleaning of HAR nanostructures, as it requires the drying of the surfaces in-between the wet cleaning and the modification steps, which is generally not possible without inducing pattern collapse. A further drawback of this method is that vapor-
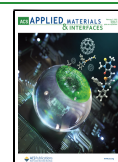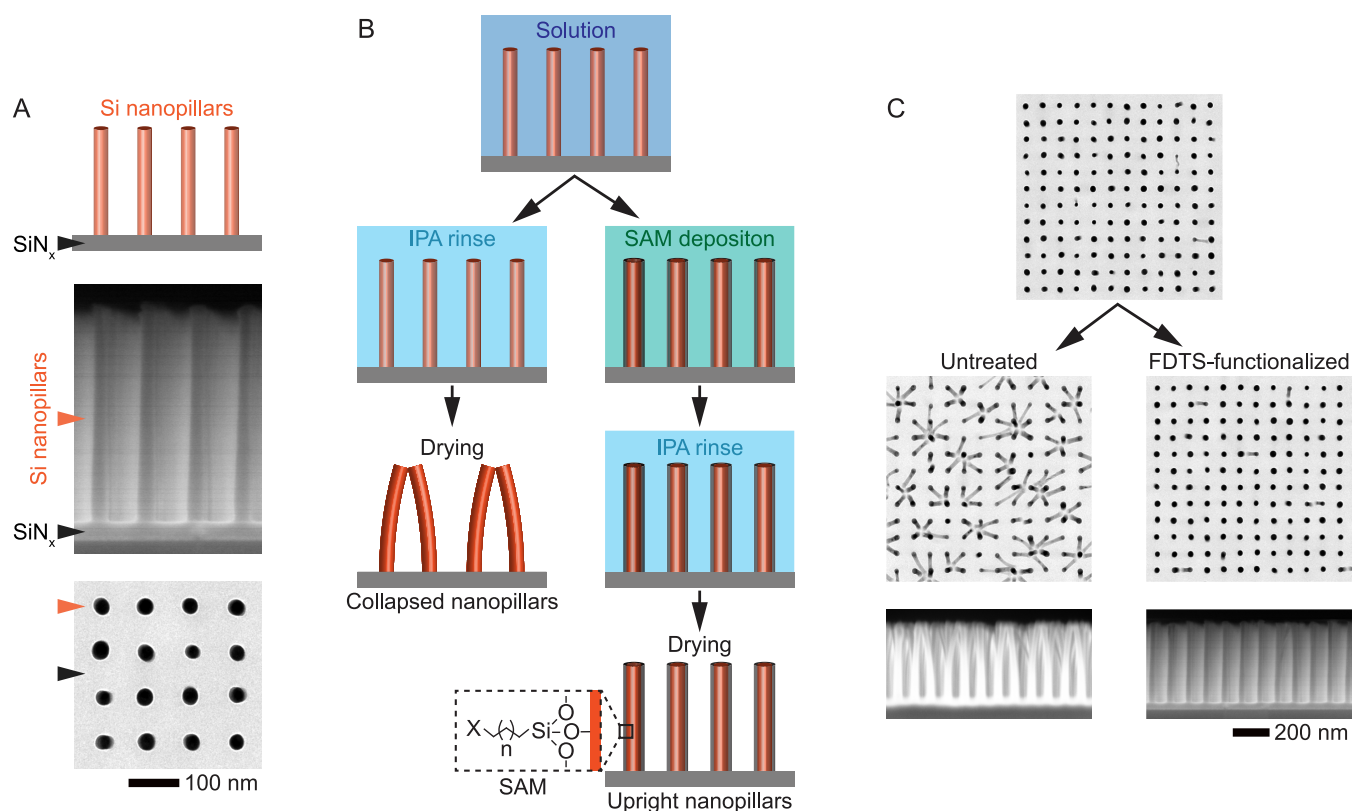
Figure 1. Liquid-phase surface chemistry modification method to prevent the collapse of high-aspect-ratio (HAR) nanopillars. (A) (*Top*) Schematic of an array of HAR Si nanopillars on a SiN$_x$ membrane, (*middle*) cross-sectional SEM, and (*bottom*) top-down transmission electron microscopy (TEM) images of 25-nm-diameter and 380-nm-tall Si nanopillars with a pitch of 90 nm, which were used to explore the pattern collapse. (B) Schematic showing collapse of untreated (*left*) and SAM-functionalized (*right*) nanopillars after rinsing in a low-surface-tension liquid (IPA). Nanopillars functionalized with 1*H*,1*H*,2*H*,2*H*-perfluorodecyltrichlorosilane (FDTS) using the liquid-phase deposition method do not collapse. (C) Top-down TEM image confirming that, in contrast to untreated Si nanopillars, FDTS-functionalized nanopillars do not collapse upon drying in IPA. Two bottom panels show corresponding side-view SEM images of untreated (*left*) and FDTS-functionalized (*right*) nanopillars after drying in IPA.

phase-deposition-based surface modification renders the nanostructures superhydrophobic, reducing the efficacy of their cleaning with aqueous solutions.[21,32] Because of the limitations of these techniques, it is necessary to develop an industrially relevant, simple, and effective method to prevent pattern collapse during wet processes, which reduces the adhesion between the nanostructures.

Here, we use HAR Si nanopillars fabricated on top of a 40-nm-thick SiN$_x$ film deposited on a 775-μm-thick Si wafer as test nanostructures (Figure 1A, Supporting Information Section 1) to demonstrate a simple approach to prevent capillary-induced pattern collapse in 380-nm-tall and 25-nm-diameter nanopillars patterned at a pitch of 90 nm (*i.e.*, their density is 1.2×10^{10} cm^{-2}). We use a solution-phase deposition method to functionalize the surface of nanopillars with SAMs (Supporting Information Section 2) to decrease the strength of interpillar adhesion, which, in turn, drastically reduces the number of collapsed nanostructures. Significantly, our approach does not require any drying step prior to the functionalization of the surface of nanopillars. After complete drying, the SAMs are easily removed from the surfaces by air-plasma treatment.

Figure 1B shows the experimental procedure for testing the capillary-induced pattern collapse in arrays of Si nanopillars. When the nanopillars were wetted with IPA (*i.e.*, immersed in an IPA solution) and dried under ambient conditions, approx.

98% of the nanopillars ended up collapsing. This indicates that the elastic restoring force is less than both the capillary force that bends the nanopillars and the adhesive force between the nanopillars, which causes them to permanently stick to each other after drying (Figure 1C). Note that IPA is one of the low-surface-tension solvents used in the semiconductor industry to reduce the capillary forces in solution-based nanofabrication processes.[21,22] Hence, to prevent pattern collapse of very fragile nanostructures, reducing the surface tension of the processing liquids is not enough, and we also have to reduce the adhesive energy between the nanopillars so that it is less than the elastic restoring force.

To control the adhesive energy between the nanopillars, we functionalized their surfaces with different silanes using the liquid-phase deposition method described in the Experimental Section. Silanes consist of a hydrolyzable group (typically alkoxy or halogen) and a functional group that mainly gives the different characteristics of surface energy. The hydrolyzable group covalently bonds to silanol groups on the surface of piranha-treated Si nanopillars (Supporting Information Section 2). Figure 1C shows an example of reduction in adhesive energy obtained by coating the nanopillar surface with 1*H*,1*H*,2*H*,2*H*-perfluorodecyltrichlorosilane (FDTS), which resulted in only 4% of the nanopillars collapsing after drying in IPA, in contrast to 98% collapse in untreated nanopillars. Note that 4% corresponds to the fraction of the collapsed as-
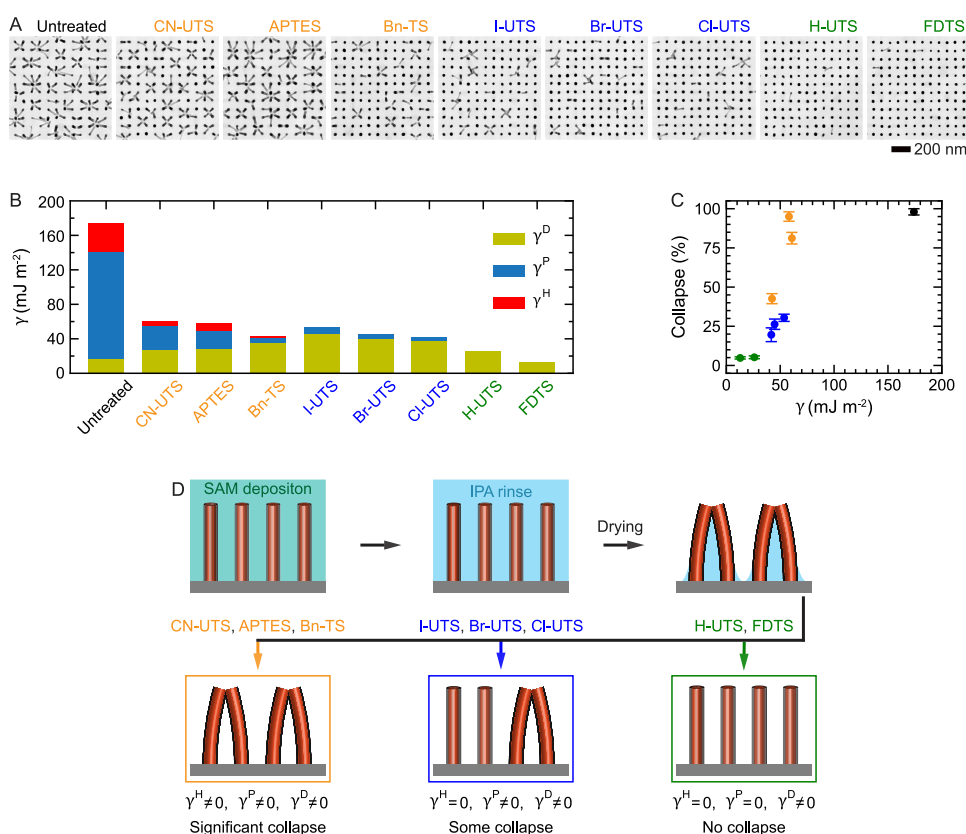
Figure 2. Pattern collapse in silane-treated nanopillars. (A) TEM images of untreated and SAM-functionalized nanopillars after IPA rinsing and drying under an ambient condition. (B) Bar plot of dispersive (γ^D), polar (γ^P), and H-bonding (γ^H) components of the surface free energies of flat Si (100) surfaces treated with the different SAMs. (C) Fraction of the collapsed nanopillars versus their measured net surface energies. The color of data points corresponds to the color of the silane groups in panel (B). (D) Schematic illustration summarizing different scenarios of the adhesion causing the pattern collapse; γ^H has the biggest impact on the interpillar adhesion and causes pattern collapse, followed by γ^P, and γ^D does not contribute to the adhesion.

fabricated nanopillars due to minor fabrication defects (Figure S1). This suggests that during the FDTS deposition and drying step, for all practical purposes, there is no pattern collapse.

To understand why FDTS prevents the collapse of these fragile nanopillars, we systematically assessed multiple silanes with different functional groups, which affect the characteristics of surface energy differently. In general, the adhesive energy between two functionalized surfaces is explained in terms of noncovalent interactions (dispersive (γ^D), polar (γ^P), and H-bonding (γ^H)) between the functionalized surfaces.[33−35] The dispersive (γ^D), polar (γ^P), and H-bonding (γ^H) components arise from the interaction of fluctuating dipoles with induced dipoles in neighboring molecules,[34] interactions between permanent dipoles,[35,36] and H-bonding between the molecules on the nanopillars coming into contact, respectively. To achieve a range of noncovalent interactions, we functionalized the nanopillars using a variety of silane-based SAMs. The individual contributions of dispersive, polar, and H-bonding components of noncovalent interactions as well as the total surface energies (γ) obtained using the extended Fowkes method[37] from SAM-functionalized flat Si (100) surfaces are summarized in Table S1 and Figure 2B. Our surface energy measurements show that the surfaces functionalized with 11-cyanoundecyltrichlorosilane (CN-UTS), 3-aminopropyltriethoxysilane (APTES), and benzyltrichlorosilane (Bn-TS) have all three surface energy components, the surfaces functionalized with 11-iodoundecyltrichlorosilane (I-UTS),

11-bromoundecyltrichlorosilane (Br-UTS), and 11-chloroundecyltrichlorosilane (Cl-UTS) have polar and dispersive components, and the surfaces functionalized with undecyltrichlorosilane (H-UTS) and 1H,1H,2H,2H-perfluorodecyltrichlorosilane (FDTS) have only dispersive components.

Next, we functionalized the nanopillars with different silanes using the liquid-phase deposition and compared how different molecules affect the capillary-induced pattern collapse by rinsing the nanopillars in IPA and drying them under ambient conditions ($T \approx 296$ K, RH $\approx 50\%$) (Figure 2A). Note that the contact angle of IPA on the FDTS-functionalized flat Si substrate was 48°, and between 5−10° for all of the other silane-treated Si surfaces (Figure S3 and Supporting Information Section 2). Hence, during drying in IPA, the capillary forces experienced by nanopillars with different silanes should be similar, i.e., after drying, one would expect to observe a similar fraction of nanopillars to collapse for all silanes, except for FDTS. However, the fractions (Figure 2C) of functionalized nanopillars that collapse for different silanes are different. This suggests that the observed collapse rates are primarily dictated by adhesion between the nanopillars and not the capillary forces.

We note that even though APTES has lower net surface energy than CN-UTS (Figure 2B), the respective fractions of nanopillars that collapsed were 95 and 81% for APTES and CN-UTS, respectively (Figure 2C). This indicates that the adhesive energy between the nanopillars depends on the

individual contribution of surface energy components γ^D, γ^P, and γ^H rather than γ. We observed that the fraction of collapsed nanopillars reduces significantly for silanes with $\gamma^H \leq 1$ mJ m^{-2} (as in the case of Bn-TS that results in 42% collapse), implying that γ^H is the most significant component of the interpillar adhesive energy.[36,38]

Next, to evaluate the contributions of γ^D and γ^P, we looked at the pattern collapse for the nanopillars functionalized with silanes that do not form H-bonds (I-UTS, Br-UTS, Cl-UTS, H-UTS, and FDTS). For I-UTS, Br-UTS, and Cl-UTS, the fraction of the nanopillars that collapsed after IPA drying was 30, 26, and 19%, respectively. However, for the silanes with no polar adhesive component, such as H-UTS, and FDTS, only about 4% of the nanopillars collapsed (Figure 2B–C). As mentioned earlier, 4% corresponds to the collapse ratio of original as-fabricated samples (Figure S1). Hence, to reduce pattern collapse, both γ^H and γ^P should be reduced, even though the contribution of γ^H to the collapse is more significant.

To test how pattern collapse differs for the nanostructures dried in water ($\sigma = 72$ mN m^{-1}), we repeated similar studies, but instead of IPA, the drying was done in water (Figures S4–S5 and Supporting information Section 3). For this case, the overall trend was similar to that shown in Figure 2A–C but different in terms of the absolute fractions of collapsed nanopillars. For example, for nanopillars coated with CN-UTS, APTES, Bn-TS, I-UTS, Br-UTS, Cl-UTS, H-UTS, and FDTS, the respective fractions of the collapsed nanopillars were 87, 98, 37, 36, 37, 29, 15, and 7%.

Our experimental results suggest that HAR nanopillars bend to form clusters irrespective of the equilibrium contact angles and surface tensions of the liquids. To validate these observations, we explored the dynamics of the cluster formation under similar experimental conditions using fluid–structure interaction (FSI) simulations (Experimental Section and Supporting Information Section 4). In our simulations, 2 × 2 silicon nanopillars of height 380 nm are fully immersed in water or IPA initially (Figure 3A), and then water or IPA is discharged out from all four directions to simulate the drying process (Figure 3B–C). We mention here that when the nanopillars deform at a very high rate in a given time step (e.g., at 12, 14, and 65 ns in Figure 3B–C), the simulation crashes as the dynamic meshing cannot keep up with the structural deformation. Hence, simulating all the way to the point at which nanopillars contact each other was not feasible. Physically when the structures deform at this rate, we assume that the nanopillars snap and form a cluster. Thus, we consider that the nanopillars already formed clusters after 12, 14, and 65 ns, as shown in Figure 3B–C.

Our simulations show that HAR nanopillars cluster both in water and in IPA, regardless of whether their surfaces are hydrophobic (Figure 3) or hydrophilic (Figure S6). However, different mechanisms were responsible for causing the cluster formation in each case. For hydrophobic nanopillars in water, when the nanopillars pierce the liquid–air interface, the receding contact angles are much lower than the equilibrium contact angles ($\theta_c = 89$ and $115°$) (Figure 3B). Before they attain their equilibrium contact angle, the nanopillars are already deformed to form clusters (Figure 3B: $t = 4$–8 ns). The receding local contact angles and resulting complex meniscus shapes cause higher dynamic interfacial forces on the nanopillars than those calculated at the equilibrium, causing clustering of the nanopillars.[39] For liquids with low surface
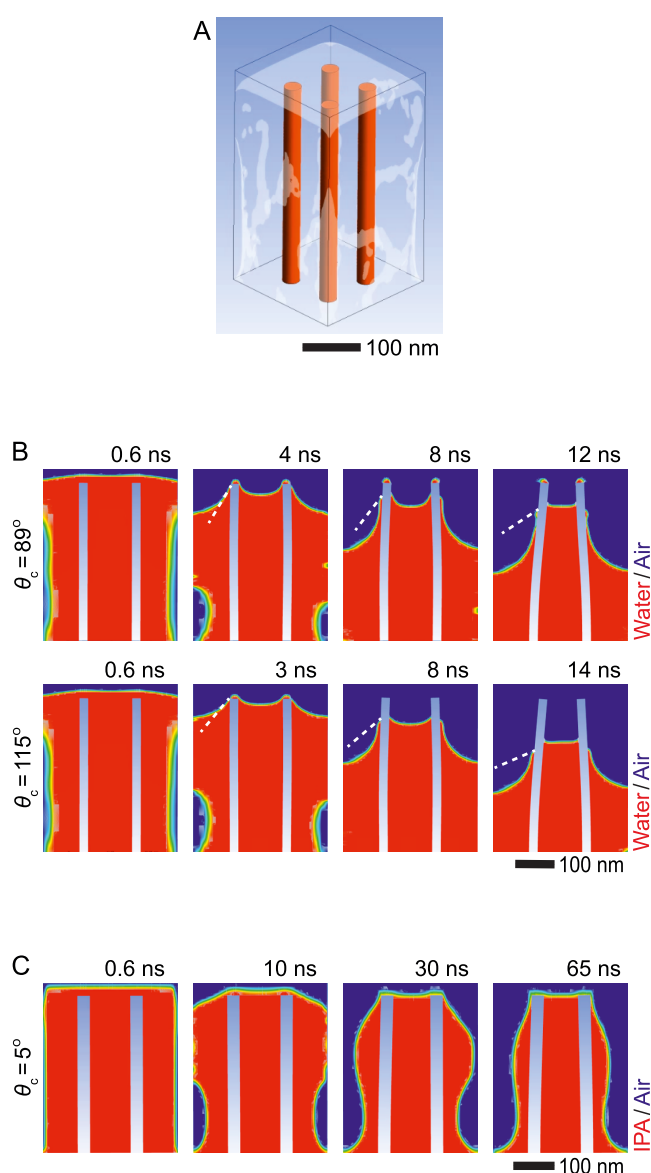

Figure 3. Fluid–structure interaction (FSI) simulation of nanopillars drying. (A) FSI simulation model showing the initial condition of the simulation. (B) Time series of the FSI simulation of the nanopillars drying in water for two contact angles (θ_c) of 89 and 115°. The time series shows the diagonal cross sections of the 2 × 2 nanopillars as the nanopillars move diagonally toward the center to form a cluster. The white dashed lines indicate the local receding contact angles with the nanopillar at the given times. The receding contact angles are much lower than the equilibrium contact angles ($\theta_c = 89$ and $115°$). For a 115° contact angle, the solid–liquid interface forms in 3 ns, which is 1 ns faster than in the case of the 89° contact angle. (C) Time series of the FSI simulation of the nanopillars drying in IPA for a contact angle of 5°. Due to higher viscosity than water and a much lower contact angle, the IPA case took much longer for the liquid to diffuse out. As IPA evaporates, a nanodroplet encapsulating the nanopillars forms before the formation of the solid–liquid–air interface. Images used courtesy of ANSYS, Inc.

tension, such as IPA, liquid wraps around the nanopillars before forming a solid–liquid–air interface, which causes the nanopillars to be trapped inside a local nanodroplet even before the nanopillars pierce the liquid–air interface (Figure 3C). At the later stage of drying, a solid–liquid–air interface might develop isolated capillary bridges; however, this would

only cause further bending of the nanopillars, causing them to cluster.[9] Furthermore, hydrophilic nanopillars in water behave similarly to those in IPA (Figure S6). Hence, our simulations confirm the experimentally observed clustering of HAR nanopillars both in water and in IPA.

To validate that the silanes uniformly coat Si surfaces, we characterized the functionalized flat surfaces of Si (100) wafers with X-ray photoelectron spectroscopy (XPS). We did not use the array of cylindrical nanopillars because of their vertical patterns. The XPS spectrum collected from an FDTS-coated flat Si wafer (Figure 4A) displays the characteristic peaks of FDTS (F 1s, FKLL), confirming the successful deposition of FDTS.[30,40] The thickness was estimated from the attenuation length of Si 2p peaks by comparing untreated and functionalized wafers. The qualitative match between the attenuation
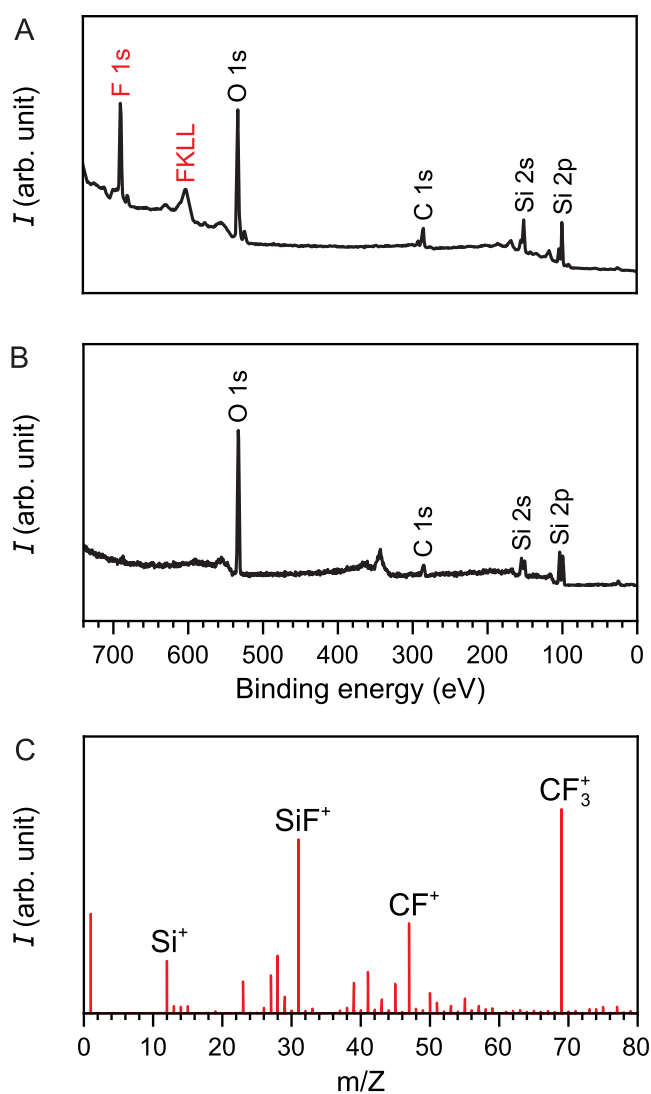
length and the thicknesses expected from the C-chain length of the surfactants confirmed the uniform deposition of SAMs (Supporting Information Section 5).

During a typical semiconductor nanofabrication process, the final Si surface after each rinsing/drying cycle should be pristine and clean of any contaminants. Hence, having an efficient approach for removing SAMs after each wet processing step is essential. We found that the FDTS monolayer can easily be removed from a Si substrate by a simple 60-s-long low-power air-plasma treatment, as confirmed by the absence of the F 1s peak after plasma cleaning (Figures 4B and S15).

While our tests on Si wafers provide a strong indication of efficient SAM functionalization of a clean Si surface, validating the presence of silanes on the surface of Si nanopillars is still important. We performed time-of-flight secondary ion mass spectrometry (TOF-SIMS) analysis directly on the FDTS-functionalized nanopillars to validate the presence of SAMs. The peaks of fluorinated CF^+ and CF_3^+ ions in the TOF-SIMS spectrum displayed in Figure 4C confirm the presence of FDTS on the nanopillars.

In conclusion, our results show that while liquids drive the clustering of nanopillars, it is the strength of interpillar adhesion that determines whether this clustering is permanent or not. Our solution-phase deposition approach to functionalize Si nanostructures with FDTS SAMs, which can disrupt these adhesions and prevent the collapse of the nanostructures, has two clear advantages: (i) the functionalization can be done during any wet processing step of fabrication without the need for drying, and (ii) the SAM can be easily cleaned after each drying step. As the semiconductor industry shifts from planar to high-density vertical nanoscale device architectures to boost the performance of microprocessors and other electronic components, new strategies that mitigate failures encountered during the different stages of nanofabrication are needed. Our approach to preventing capillary-induced pattern collapse provides a simple and efficient method that can enable damage-free fabrication of smaller and densely packed vertical nanostructures.

Figure 4. XPS and time-of-flight secondary ion mass spectrometry (TOF-SIMS) studies. (A) XPS spectrum from an FDTS-functionalized Si (100) surface. F 1s and FKLL peaks confirm the presence of FDTS on the surface. (B) XPS spectrum after air-plasma treatment of the FDTS-functionalized Si surface. The absence of F 1s and FKLL peaks confirms that FDTS molecules were effectively removed from the surface by plasma cleaning. (C) TOF-SIMS spectrum obtained directly from the nanopillars functionalized with FDTS displays characteristic peaks (CF^+ and CF_3^+) associated with FDTS.

■ EXPERIMENTAL SECTION

Fabrication of Chips Containing an Array of Nanopillars. Nanopillars (380 nm in height, 25 nm in diameter, and 90 nm in pitch) were patterned on one side of a 775-μm-thick Si (100) wafer with a 40-nm-thick SiN_x film, from which the chips of dimensions 6.15 mm × 5.1 mm were fabricated. The viewing window was patterned and etched from the other side of the wafer using photolithography, deep reactive ion etching (DRIE), and KOH etching. The fabrication process of these chips is briefly described in Supporting Section 1 and in more detail in our earlier studies.[7,17]

Liquid-Phase Silane Deposition. The chips with nanopillars were air-plasma-treated for 10 min and then immersed into a freshly prepared piranha solution, a H_2SO_4/H_2O_2 (3:1 volume ratio) mixture, for 30 min to generate hydroxyl functions on the surface. Afterward, these chips were rinsed in water, IPA, and toluene, and then the chips were immersed in a freshly prepared silane solution containing 10 μL of silane and 10 mL of toluene for 30 min. The silanes anchor on the surface of nanopillars via $Si_{silane}-O-Si_{surface}$ bonding, forming a monolayer around the nanopillars.[41] Next, the chips were first rinsed with toluene, and then with IPA (Figure 2) or water (Figure S5) and dried under ambient conditions ($T \approx 296$ K, RH $\approx 50\%$) to study the collapse of nanopillars. Further details on the silane deposition method are described in Supporting Information Section 2.

Contact Angle Measurement. During the deposition of silane on a chip with nanopillars, a flat Si (100) piece also went through the same treatment as a control sample. We used the silane-treated flat Si (100) piece to assess the effect of the silane functionalization by measuring the contact angles to gauge the surface wettability (*i.e.*, hydrophilicity/hydrophobicity of the surfaces). Using OCA25 (DataPhysics Instruments, Germany) and DSA25 (KRÜSS GmbH, Germany) systems, we measured contact angles for both IPA and water on Si (100) surfaces treated with different silanes, which are summarized in Figures S3−S4.

Surface Free Energy Measurement. We measured surface free energies of different silane-treated surfaces using the extended Fowkes method.[37] Here, the surface free energy is divided into dispersive (γ^D), polar (γ^P), and H-bonding (γ^H) components, which are related to the corresponding components in a given liquid and the contact angle by the following equation

$$\left(\sqrt{\gamma^D \gamma_l^D} + \sqrt{\gamma^P \gamma_l^P} + \sqrt{\gamma^H \gamma_l^H}\right) = \frac{1}{2}\gamma_l(1 + \cos\theta_c) \tag{1}$$

where γ_l^D, γ_l^P, and γ_l^H are dispersive, polar, and H-bonding components of liquid's surface energy, θ_c is the contact angle, and γ_l is the surface tension of the liquid. To solve the equation and calculate the individual surface free energy components of a silane-treated surface, we measure the contact angles for water, ethylene glycol, and diiodomethane. From the known values of their surface energy components and the measured values of the corresponding contact angles, we calculated the surface energy components of the silane-treated surfaces, which are presented in Table S1 and Figure 2B.

TEM Imaging. We used a JEOL 2010FEG TEM (JEOL Ltd., Tokyo, Japan) operated at an accelerating voltage of 200 kV and equipped with a Gatan OneView camera (Gatan Inc., Pleasanton, CA) to acquire the TEM images of the nanopillars after drying in IPA or water. These TEM images were used to analyze the fraction of collapsed nanopillars.

FSI Simulations. Fluid−structure interaction (FSI) is a multiphysics coupling between fluid dynamics and structural mechanics. One-way FSI solves the fluid flow first, and the fluid pressure exerted on the structure is passed to the structural solver. Though the one-way FSI is useful for simple cases, in reality, the structure deformation would, in return, trigger changes in the fluid flow, which goes unaccounted here. Hence, a two-way interactive coupling between the systems, where the fluid solver calculates the pressure on the structure and the structure solver calculates the deformation for the fluid flow, is required to capture the complete dynamics of the interaction. Two-way FSI simulations were performed with the ANSYS multiphysics software package (*i.e.*, fluent and mechanical).[42] The volume of fluid (VOF) method was used to simulate the multiphase fluid flow, and the dynamic meshing was employed to accommodate the nanopillars deformation. The simulations were carried out with a time step of 8 ps and at a temperature of 300 K. We have simulated simple cases with four (*i.e.*, 2×2) nanopillars on a cuboidal enclosure. The four sides of the enclosures served as pressure outlets for the liquid, and the liquid was diffused out from these outlets to simulate the drying process. The nanopillar dimensions, contact angle, and corresponding fluid properties were chosen accordingly for each case. We initialized the simulation with an air−liquid interface over the top of the nanopillars. The structural solver (mechanical) solves how forces from the fluid flow exerted on the structure deform the structure, and a fluid flow solver (fluent) simulates how the structural deformations and the fluid drying affect the flow. Both solvers are coupled to transfer the force and deformation data sequentially at every time step. Iteratively they converge to a solution for every time step before they simulate the next time step. We have simulated the drying of the nanopillars for the following cases: (I) 21-nm-diameter and 380-nm-tall nanopillars in water for two contact angles of 89 and 115° (Figure 3B); (II) 30-nm-diameter and 380-nm-tall nanopillars in IPA for contact angles of 5° (Figure 3C); and (III) 30-nm-diameter and 350-nm-tall nanopillars in water for contact angles of 5° (Figure S6). Each of these cases shows that the nanopillars bend sufficiently to come into contact and cluster with each other. We have intentionally chosen stiffer nanopillars for

5°-contact angle cases to show that even the nanopillars with relatively higher rigidity bend and form clusters, which suggests that the softer nanopillars, *i.e.*, 21-nm-diameter and 380-nm-tall nanopillars, will form cluster as well.

XPS Measurements. X-ray photoelectron spectroscopy (XPS) measurements were performed using an Omicron EA125 U7 hemispherical electron spectrometer with seven-channel detection installed on the VG Scientific ESCA Lab Mark 2 chamber. XPS spectra were recorded using Omicron Twin Anode X-ray Mg Kα excitation at 300 W (15 kV × 20 mA). The pressure during XPS measurement was in the 10^{-9} Torr range. The analyzer pass energy was set at 80 eV for survey scans and 20 eV for high-resolution scans. The sample was positioned perpendicular to the detector and kept at room temperature during the measurements. The binding energy scales were furthermore corrected for charging, using C 1s = 284.6 eV as a reference. Detailed results are discussed in Supporting Information Section 5.

TOF-SIMS Measurements. We used TOF.SIMS 5 (ION-TOF, GmbH, Muenster, Germany) to conduct time-of-flight secondary ion mass spectrometry (TOF-SIMS) directly on silane-treated nanopillars in a high mass resolution mode (with a lateral resolution of approx. 3 μm and information depth of 1−5 nm). The primary ion source of 30 keV Bi$_3^+$ was used for the analysis with a very low ion dose (<10^{13} ions/cm^2) (Figure 4C).

■ ASSOCIATED CONTENT

Ⓢ Supporting Information

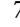The Supporting Information is available free of charge at https://pubs.acs.org/doi/10.1021/acsami.1c17781.

Additional materials and methods used in our study and discussions on modeling and analysis (PDF)

■ AUTHOR INFORMATION

Corresponding Authors

XiuMei Xu − *imec, Leuven B-3001, Belgium;*
   Email: XiuMei.Xu@imec.be

Christian A. Nijhuis − *Department of Chemistry, National University of Singapore, Singapore 117543, Singapore; Centre for Advanced 2D Materials and Graphene Research Centre, National University of Singapore, Singapore 117546, Singapore; Hybrid Materials for Opto-Electronics Group, Department of Molecules and Materials, MESA+ Institute for Nanotechnology and Center for Brain-Inspired Nano Systems, Faculty of Science and Technology, University of Twente, 7500 AE Enschede, The Netherlands;* ⓞ orcid.org/0000-0003-3435-4600; Email: c.a.nijhuis@utwente.nl

Utkur Mirsaidov − *Department of Physics, National University of Singapore, Singapore 117551, Singapore; Centre for BioImaging Sciences, Department of Biological Sciences, National University of Singapore, Singapore 117557, Singapore; Centre for Advanced 2D Materials and Graphene Research Centre, National University of Singapore, Singapore 117546, Singapore; Department of Materials Science and Engineering, National University of Singapore, Singapore 117575, Singapore;* ⓞ orcid.org/0000-0001-8673-466X; Email: mirsaidov@nus.edu.sg

Authors

Tanmay Ghosh − *Department of Physics, National University of Singapore, Singapore 117551, Singapore; Centre for BioImaging Sciences, Department of Biological Sciences, National University of Singapore, Singapore 117557, Singapore;* ⓞ orcid.org/0000-0003-0532-2407

Eva-Corinna Fritz − *Department of Chemistry, National University of Singapore, Singapore 117543, Singapore*

Deepan Balakrishnan − *Centre for BioImaging Sciences, Department of Biological Sciences, National University of Singapore, Singapore 117557, Singapore*

Ziyu Zhang − *Department of Chemistry, National University of Singapore, Singapore 117543, Singapore*

Nandi Vrancken − *imec, Leuven B-3001, Belgium; Department of Materials & Chemistry, Vrije Universiteit Brussel, Brussel B-1050, Belgium*

Utkarsh Anand − *Department of Physics, National University of Singapore, Singapore 117551, Singapore; Centre for BioImaging Sciences, Department of Biological Sciences, National University of Singapore, Singapore 117557, Singapore;* orcid.org/0000-0003-3914-8435

Hong Zhang − *Department of Chemistry, National University of Singapore, Singapore 117543, Singapore*

N. Duane Loh − *Department of Physics, National University of Singapore, Singapore 117551, Singapore; Centre for BioImaging Sciences, Department of Biological Sciences, National University of Singapore, Singapore 117557, Singapore*

Frank Holsteyns − *imec, Leuven B-3001, Belgium*

Complete contact information is available at:
https://pubs.acs.org/10.1021/acsami.1c17781

Notes
The authors declare no competing financial interest.

■ REFERENCES

(1) Pint, C. L.; Takei, K.; Kapadia, R.; Zheng, M.; Ford, A. C.; Zhang, J.; Jamshidi, A.; Bardhan, R.; Urban, J. J.; Wu, M.; Ager, J. W.; Oye, M. M.; Javey, A. Rationally Designed, Three-Dimensional Carbon Nanotube Back-Contacts for Efficient Solar Devices. *Adv. Energy Mater.* **2011**, *1*, 1040−1045.

(2) Mor, G. K.; Shankar, K.; Paulose, M.; Varghese, O. K.; Grimes, C. A. Use of Highly-Ordered TiO2 Nanotube Arrays in Dye-Sensitized Solar Cells. *Nano Lett.* **2006**, *6*, 215−218.

(3) Fachin, F.; Chen, G. D.; Toner, M.; Wardle, B. L. Integration of Bulk Nanoporous Elements in Microfluidic Devices with Application to Biomedical Diagnostics. *J. Microelectromech. Syst.* **2011**, *20*, 1428−1438.

(4) De Volder, M.; Hart, A. J. Engineering Hierarchical Nanostructures by Elastocapillary Self-Assembly. *Angew. Chem., Int. Ed.* **2013**, *52*, 2412−2425.

(5) Kuhn, K. J. Considerations for Ultimate CMOS Scaling. *IEEE Trans. Electron Devices* **2012**, *59*, 1813−1828.

(6) Zhao, X.; Lin, J.; Heidelberger, C.; Fitzgerald, E. A.; Alamo, J. A. d. In *Vertical Nanowire InGaAs MOSFETs Fabricated by a Top-Down Approach*, 2013 IEEE International Electron Devices Meeting, 9−11 Dec. 2013, 2013; pp 28.4.1−28.4.4.

(7) Aabdin, Z.; Xu, X. M.; Sen, S.; Anand, U.; Král, P.; Holsteyns, F.; Mirsaidov, U. Transient Clustering of Reaction Intermediates During Wet Etching of Silicon Nanostructures. *Nano Lett.* **2017**, *17*, 2953−2958.

(8) Şengül, H.; Theis, T. L.; Ghosh, S. Toward Sustainable Nanoproducts. *J. Ind. Ecol.* **2008**, *12*, 329−359.

(9) Chandra, D.; Yang, S. Capillary-Force-Induced Clustering of Micropillar Arrays: Is It Caused by Isolated Capillary Bridges or by the Lateral Capillary Meniscus Interaction Force? *Langmuir* **2009**, *25*, 10430−10434.

(10) Pokroy, B.; Kang, S. H.; Mahadevan, L.; Aizenberg, J. Self-Organization of a Mesoscale Bristle into Ordered, Hierarchical Helical Assemblies. *Science* **2009**, *323*, 237−240.

(11) Tanaka, T.; Morigami, M.; Atoda, N. Mechanism of Resist Pattern Collapse During Development Process. *Jpn. J. Appl. Phys.* **1993**, *32*, 6059−6064.

(12) Roman, B.; Bico, J. Elasto-Capillarity: Deforming an Elastic Structure with a Liquid Droplet. *J. Phys.: Condens. Matter* **2010**, *22*, 493101.

(13) Chang, C.-C.; Wang, Z.; Sheng, Y.-J.; Tsao, H.-K. Nanostructure Collapse by Elasto-Capillary Instability. *Soft Matter* **2014**, *10*, 8542−8547.

(14) Kim, I.; Mun, J.; Hwang, W.; Yang, Y.; Rho, J. Capillary-Force-Induced Collapse Lithography for Controlled Plasmonic Nanogap Structures. *Microsyst. Nanoeng.* **2020**, *6*, 65.

(15) Duan, H.; Yang, J. K. W.; Berggren, K. K. Controlled Collapse of High-Aspect-Ratio Nanostructures. *Small* **2011**, *7*, 2661−2668.

(16) Lao, Z.; Pan, D.; Yuan, H.; Ni, J.; Ji, S.; Zhu, W.; Hu, Y.; Li, J.; Wu, D.; Chu, J. Mechanical-Tunable Capillary-Force-Driven Self-Assembled Hierarchical Structures on Soft Substrate. *ACS Nano* **2018**, *12*, 10142−10150.

(17) Vrancken, N.; Ghosh, T.; Anand, U.; Aabdin, Z.; Chee, S. W.; Baraissov, Z.; Terryn, H.; Gendt, S. D.; Tao, Z.; Xu, X.; Holsteyns, F.; Mirsaidov, U. Nanoscale Elastocapillary Effect Induced by Thin-Liquid-Film Instability. *J. Phys. Chem. Lett.* **2020**, *11*, 2751−2758.

(18) Grinthal, A.; Kang, S. H.; Epstein, A. K.; Aizenberg, M.; Khan, M.; Aizenberg, J. Steering Nanofibers: An Integrative Approach to Bio-Inspired Fiber Fabrication and Assembly. *Nano Today* **2012**, *7*, 35−52.

(19) Kang, S. H.; Pokroy, B.; Mahadevan, L.; Aizenberg, J. Control of Shape and Size of Nanopillar Assembly by Adhesion-Mediated Elastocapillary Interaction. *ACS Nano* **2010**, *4*, 6323−6331.

(20) Matsunaga, M.; Aizenberg, M.; Aizenberg, J. Controlling the Stability and Reversibility of Micropillar Assembly by Surface Chemistry. *J. Am. Chem. Soc.* **2011**, *133*, 5545−5553.

(21) Xu, X. M.; Vrancken, N.; Vereecke, G.; Suhard, S.; Pourtois, G.; Holsteyns, F. Some Critical Issues in Pattern Collapse Prevention and Repair. *Solid State Phenomena* **2016**, *255*, 147−151.

(22) Eom, D.; Kim, K.; Shin, Y. Drying Performance of Single IPA Dryer to Prevent Pattern Collapse and Watermark. *ECS Trans.* **2011**, *41*, 197−204.

(23) Vrancken, N.; Vereecke, G.; Bal, S.; Sergeant, S.; Doumen, G.; Holsteyns, F.; Terryn, H.; de Gendt, S.; Xu, X. M. Pattern Collapse of High-Aspect-Ratio Silicon Nanostructures − A Parametric Study. *Solid State Phenomena* **2016**, *255*, 136−140.

(24) Bray, D. F.; Bagu, J.; Koegler, P. Comparison of Hexamethyldisilazane (HMDS), Peldri II, and Critical-Point Drying Methods for Scanning Electron Microscopy of Biological Specimens. *Microsc. Res. Tech.* **1993**, *26*, 489−495.

(25) Namatsu, H.; Yamazaki, K.; Kurihara, K. Supercritical Drying for Nanostructure Fabrication Without Pattern Collapse. *Microelectron. Eng.* **1999**, *46*, 129−132.

(26) Supekar, S. D.; Skerlos, S. J. Supercritical Carbon Dioxide in Microelectronics Manufacturing: Marginal Cradle-to-grave Emissions. *Procedia CIRP* **2014**, *15*, 461−466.

(27) Doms, M.; Feindt, H.; Kuipers, W. J.; Shewtanasoontorn, D.; Matar, A. S.; Brinkhues, S.; Welton, R. H.; Mueller, J. Hydrophobic Coatings for MEMS Applications. *J. Micromech. Microeng.* **2008**, *18*, 055030.

(28) Parvais, B.; Pallandre, A.; Jonas, A. M.; Raskin, J. Liquid and Vapor Phase Silanes Coating for the Release of Thin Film MEMS. *IEEE Trans. Device Mater. Reliab.* **2005**, *5*, 250−254.

(29) Ashurst, W. R.; Carraro, C.; Maboudian, R. Vapor Phase Anti-Stiction Coatings for MEMS. *IEEE Trans. Device Mater. Reliab.* **2003**, *3*, 173−178.

(30) Ashurst, W. R.; Carraro, C.; Maboudian, R.; Frey, W. Wafer Level Anti-Stiction Coatings for MEMS. *Sens. Actuators, A* **2003**, *104*, 213−221.

(31) Chen, B.; Seidel, S.; Hori, H.; Gupta, M. Self-Assembly of Pillars Modified with Vapor Deposited Polymer Coatings. *ACS Appl. Mater. Interfaces* **2011**, *3*, 4201−4205.

(32) Xu, X.; Vereecke, G.; Chen, C.; Pourtois, G.; Armini, S.; Verellen, N.; Tsai, W.-K.; Kim, D.-W.; Lee, E.; Lin, C.-Y.; Van Dorpe, P.; Struyf, H.; Holsteyns, F.; Moshchalkov, V.; Indekeu, J.; De Gendt, S. Capturing Wetting States in Nanopatterned Silicon. *ACS Nano* **2014**, *8*, 885−893.

(33) Fowkes, F. M. Determination of Interfacial Tensions, Contact Angles, and Dispersion Forces in Surfaces by Assuming Additivity of Intermolecular Interactions in Surfaces. *J. Phys. Chem. A* **1962**, *66*, 382.

(34) Fowkes, F. M. Attractive Forces at Interfaces. *Ind. Eng. Chem.* **1964**, *56*, 40−52.

(35) Fowkes, F. M.; Mostafa, M. A. Acid-Base Interactions in Polymer Adsorption. *Ind. Eng. Chem. Prod. Res. Dev.* **1978**, *17*, 3−7.

(36) Lee, L.-H. *Fundamentals of Adhesion*; Springer Science & Business Media: New York, 1991.

(37) Jie-Rong, C.; Wakida, T. Studies on the Surface Free Energy and Surface Structure of PTFE Film Treated with Low Temperature Plasma. *J. Appl. Polym. Sci.* **1997**, *63*, 1733−1739.

(38) Israelachvili, J. *Intermolecular and Surface Forces*, 3rd ed.; Elsevier/Academic: Amsterdam, 2011.

(39) Garcia-Gonzalez, D.; Snoeijer, J.; Kappl, M.; Butt, H.-J. Onset of Elasto-Capillary Bundling of Micropillar Arays: A Direct Visualization. *Langmuir* **2020**, *36*, 11581−11588.

(40) Fréchette, J.; Maboudian, R.; Carraro, C. Thermal Behavior of Perfluoroalkylsiloxane Monolayers on the Oxidized Si(100) Surface. *Langmuir* **2006**, *22*, 2726−2730.

(41) Akram Raza, M.; Kooij, E. S.; van Silfhout, A.; Poelsema, B. Superhydrophobic Surfaces by Anomalous Fluoroalkylsilane Self-Assembly on Silica Nanosphere Arrays. *Langmuir* **2010**, *26*, 12962−12972.

(42) Chimakurthi, S. K.; Reuss, S.; Tooley, M.; Scampoli, S. ANSYS Workbench System Coupling: A State-of-the-Art Computational Framework for Analyzing Multiphysics Problems. *Eng. Comput.* **2018**, *34*, 385−411.

📖 Recommended by ACS